Farfield pattern and guided-mode extraction analysis for highly directional emission from photonic-crystal based AlGaInP/InGaP MQW color-converters in thin-film geometry

Amade Ndiaye, Hai Son Nguyen, Christian Seassal, Emmanuel Drouard, Badhise Ben Bakir

▶ **To cite this version:**

Amade Ndiaye, Hai Son Nguyen, Christian Seassal, Emmanuel Drouard, Badhise Ben Bakir. Farfield pattern and guided-mode extraction analysis for highly directional emission from photonic-crystal based AlGaInP/InGaP MQW color-converters in thin-film geometry. AIP Advances, 2022, 12 (4), pp.045122. 10.1063/5.0085930 . hal-03708281

HAL Id: hal-03708281
https://hal.science/hal-03708281

Submitted on 23 Sep 2022

HAL is a multi-disciplinary open access archive for the deposit and dissemination of scientific research documents, whether they are published or not. The documents may come from teaching and research institutions in France or abroad, or from public or private research centers.

L'archive ouverte pluridisciplinaire **HAL**, est destinée au dépôt et à la diffusion de documents scientifiques de niveau recherche, publiés ou non, émanant des établissements d'enseignement et de recherche français ou étrangers, des laboratoires publics ou privés.

Distributed under a Creative Commons Attribution 4.0 International License

AIP Advances

Farfield pattern and guided-mode extraction analysis for highly directional emission from photonic-crystal based AlGaInP/InGaP MQW color-converters in thin-film geometry

Cite as: AIP Advances **12**, 045122 (2022); https://doi.org/10.1063/5.0085930
Submitted: 22 February 2022 • Accepted: 28 March 2022 • Published Online: 20 April 2022

Amade Ndiaye, Hai Son Nguyen, Christian Seassal, et al.

COLLECTIONS

This paper was selected as an Editor's Pick

View Online Export Citation CrossMark

ARTICLES YOU MAY BE INTERESTED IN

Development of microLED
Applied Physics Letters **116**, 100502 (2020); https://doi.org/10.1063/1.5145201

High-temperature electroluminescence properties of InGaN red 40×40 μm^2 micro-light-emitting diodes with a peak external quantum efficiency of 3.2%
Applied Physics Letters **119**, 231101 (2021); https://doi.org/10.1063/5.0070275

Red InGaN micro-light-emitting diodes (>620 nm) with a peak external quantum efficiency of 4.5% using an epitaxial tunnel junction contact
Applied Physics Letters **120**, 121102 (2022); https://doi.org/10.1063/5.0086912

AIP Advances
Nanoscience Collection
READ NOW!

© 2022 Author(s).

Farfield pattern and guided-mode extraction analysis for highly directional emission from photonic-crystal based AlGaInP/InGaP MQW color-converters in thin-film geometry

Cite as: AIP Advances 12, 045122 (2022); doi: 10.1063/5.0085930
Submitted: 22 February 2022 • Accepted: 28 March 2022 •
Published Online: 20 April 2022

View Online Export Citation CrossMark

Amade Ndiaye,[1,2,a] Hai Son Nguyen,[2] Christian Seassal,[2] Emmanuel Drouard,[2] and Badhise Ben Bakir[1,a]

AFFILIATIONS

[1] University Grenoble Alpes, CEA, LETI, MINATEC Campus, CEA-Grenoble, F38054 Grenoble, France
[2] Univ. Lyon, Institut des Nanotechnologies de Lyon-INL, UMR CNRS 5270, CNRS, Ecole Centrale de Lyon, Ecully F-69134, France

[a] **Authors to whom correspondence should be addressed:** amade.ndiaye@cea.fr and badhise.ben-bakir@cea.fr

ABSTRACT

This paper provides novel design guidelines for highly directional emission from PhC-based AlGaInP/InGaP MQW color converters (CC) in a thin-film geometry through an in-depth analysis of the measured azimuthal and spectrally resolved farfield emission patterns and a modal analysis based on coupled-mode theory and a herein-developed model for quantifying the spontaneous emission distribution between guided modes. The fabricated CC can exhibit directionality up to ~5 times higher than that of Lambertian emitters close to normal incidence. We believe that all the novel insights set through our analyses help in properly controlling the emission directionality from photonic-crystal-based MQW CC at the display level, which would eliminate the need for additional external optics. This could pave the way for the use of MQW CC to achieve compact full-color microdisplays on a single wafer.

© 2022 Author(s). All article content, except where otherwise noted, is licensed under a Creative Commons Attribution (CC BY) license (http://creativecommons.org/licenses/by/4.0/). https://doi.org/10.1063/5.0085930

I. INTRODUCTION

Color conversion is a key-technology strategy for many applications in the field of optoelectronics, e.g., solid-state lighting,[1–3] optical communication,[4] and, most recently, displays.[5–7] Particularly in display applications, it has been foreseen as a credible alternative to native RGB emission on the same substrate for achieving monolithic full-color microdisplays.[8] State-of-the-art color-conversion based microdisplays use semiconductor quantum dots (Q-dots), which suffer from photostability issues and low light absorption in the blue spectral range leading to color converters (CC) with thicknesses larger than 5 μm.[8,9] The former makes them not compatible with applications involving very high luminance (need for photostability), while the latter may cause aspect ratio issues for pixel lateral sizes under 5 μm, typical in microdisplays.[10] Therefore, inorganic MQW semiconductor color converters (CC) could gain a lot of ground due to their better photostability and higher blue light absorption.[4,8] However, their practical use for microdisplays has not been implemented yet because of their low light extraction efficiency (LEE) inherent to their high refractive indices, which drastically limits their conversion efficiencies.

Besides, additional application-driven requirements have to be taken into account, in particular for microdisplays where the resolution is a key-element in the product development. Indeed, in such applications, pixel lateral sizes can be less than 5 μm, which means that not only most of the emitted light must be extracted out of the CC, but also the extraction length (the lateral extent needed to extract most of the guided light) needs to be shorter than the pixel lateral size.[11] In addition, the next generation of near-eye microdisplay applications such as virtual, augmented, and mixed reality requires image sources with directional emission to eliminate the need for additional external optics, which tends to make

© Author(s) 2022

them heavy and bulky.[12,13] All the aforementioned issues have to be circumvented in order for the inorganic MQW semiconductor CC to become credible alternatives to Q-dots in microdisplay applications involving very high luminance (need for photostability) and compact integration schemes (need for CC with thickness <5 μm).

Photonic crystals (PhCs), which are periodic dielectric modulations at wavelength-scale, have already been widely applied to enhance LEE in high refractive-index materials.[14–17] In addition, it has also been shown that they could exhibit strong interaction with guided Bloch modes when combined with thin-film devices, which could lead to very short extraction lengths.[18] In a recent study, our group has reported on the first PhC based AlGaInP/InGaP MQW CC fully optimized for blue-to-red and green-to-red color conversions in microdisplays. The thickness of the epitaxial layer was around 600 nm and we demonstrated that with PhCs etched at around a third of the total thickness, quasi-complete light-outcoupling could be achieved within very short extraction lengths (<3 μm), far shorter than any other characteristic lengths.[19]

Due to the coherent nature of their diffraction processes, PhCs are also able to directly shape farfield patterns to achieve directional emission and super-Lambertian emission (more directional than Lambertian emission) has already been reported in various devices, mostly light-emitting diodes (LEDs). However, the large number of guided-modes due to their thick epitaxial structures and metal absorption due to the presence of metallic layers for electrical injection made the guided-mode identification very tricky and left only a little room for achieving highly directional emission.[18,20–22] AlGaInP/InGaP MQW CC, on the other hand, have different characteristics than LEDs. Indeed, their epitaxial layers can be made thinner (<1 μm, supporting a lower number of guided modes) and they can be fabricated as stand-alone structures on transparent substrates (no metal absorption).[19] In the framework of color conversion, using PhCs could thus be an interesting route to properly engineer the directionality of the emission at the display level through a better control of the guided-mode extraction, which is still one of the key issues in our targeted applications.[23]

This paper provides novel design guidelines for highly directional emission from PhC-based AlGaInP/InGaP MQW CC in thin-film geometry through an in-depth analysis of the measured azimuthal and spectrally resolved farfield emission patterns and a modal analysis based on coupled-mode theory and a herein-developed model for quantifying the spontaneous emission distribution between guided modes. The paper is organized as follows: Sec. II outlines the fabricated structures and the measurement setup used for farfield emission pattern measurements, while Sec. III defines the key figure of merit (FoM) to assess the directionality of an emitter. The experimental results are analyzed in Sec. IV, proposing a thorough design methodology to achieve highly directional emission from MQW CC and highlighting some novel design guidelines for such structures.

II. EXPERIMENTAL DETAILS

A. Fabricated structures

The AlGaInP epitaxial structure (see Table I) is transferred onto a transparent substrate using oxide-mediated molecular bonding with a high bonding yield[24] [>90% as shown in Fig. 1(a)].

The GaAs substrate and layers 1, 2, and 3 were subsequently removed using highly selective wet etching techniques. The thickness of the remaining CC is, therefore, ~600 nm, which is enough for complete blue light absorption. The PhC patterns were subsequently defined using e-beam lithography followed by RIE etching techniques. A detailed flow chart of all the fabrication steps is provided in the supplementary material (Note I) for more information.

Square lattices with two different types of patterns have been fabricated: a square lattice of air holes and a square lattice of nanopillars. In the following, they will be referred to as holes and pillars, respectively. Square lattices are chosen to match the square geometry of the mesas formed by the μ-Leds in a 2D array configuration for microdisplay applications. PhCs were etched at around one third of the total thickness of the epitaxial structures to ensure efficient coupling between the guided Bloch-modes supported by our CC and the PhC patterns.[19] Besides, the lateral extent of all PhCs were chosen to be 100 periods so that the CC can be considered laterally "infinite." Indeed, their lateral extents are far longer than the extraction lengths of the PhCs, which are less than 3 μm in the range of our lattice periods.[19]

For each pattern type, different structures with different lattice periods have been considered: lattice periods from 400 to 550 nm with a step of 50 nm. The lower and upper limits are to ensure that (i) each of the guided modes supported by our CC can be prone to diffraction into air and (ii) there can be enough diffractive elements in pixels whose lateral dimensions are compatible with the high-resolution of μ-Led displays.[19]

In Figs. 1(b)–1(d), a cross section of the color-converter on a transparent substrate and scanning electron microscopy (SEM) images of some of the fabricated structures are displayed.

B. Measurement setup for back focal plane imaging

We use back focal plane (BFP) imaging[25,26] to properly analyze the radiation pattern properties of the PhC-based CC. In this framework, a 405 nm laser line was focused on the sample at normal incidence by a microscope objective (MO) called the excitation objective with NA = 0.75. This numerical aperture is enough to collect most of (>85%) the emitted light and evaluate the directionality of our PhC-based CC due to the highly directional nature of their emission (see Sec. IV and Ref. 19). The photoluminescence (PL) signals were collected by the same excitation objective.

To evaluate the directionality of our structures, we first measure the 2D momentum space (k_x, k_y) distribution of the PL signal emitted from the CC and integrated over the whole emission spectrum by directly collecting the image of the BFP with a CCD camera. This corresponds to the so-called azimuthal farfield radiation patterns and will be plotted in polar coordinates in the following sections, as displayed in Fig. 2(a).

Next, to have a better insight into the guided-mode extraction, we measure the energy–momentum dispersion diagram of our PhC-based CC by using an entrance slit [see Fig. 2(b)]. This provides the so-called spectrally resolved farfield patterns which are collected along the ΓX direction of our structures. More details about the experimental setup can be found in the supplementary material (Note II).

© Author(s) 2022

TABLE I. III-V epitaxial growth layer structure and characteristics.

Layer	Material	Thickness
0: Substrate	GaAs	625 μm
1: Buffer layer	U-GaAs	200 nm
2: Etch-stop layer	U-InGaP	300 nm
3: Sacrificial layer	U-GaAs	50 nm
4: Cladding	U-$(Al_{x2}Ga_{1-x2})_{0.52}In_{0.48}P$	200 nm
5: MQW barrier	U-$(Al_{x1}Ga_{1-x1})_{0.52}In_{0.48}P$	70 nm
6: MQW region	4×U-$In_yGa_{1-y}P$/ 5×U-$(Al_{x1}Ga_{1-x1})_{0.52}In_{0.48}P$	4.4 nm/8.7 nm
7: MQW barrier	U-$(Al_{x1}Ga_{1-x1})_{0.52}In_{0.48}P$	70 nm
8: Cladding	U-$(Al_{x2}Ga_{1-x2})_{0.52}In_{0.48}P$	200 nm
9: Bonding interface	U-GaAs	20 nm

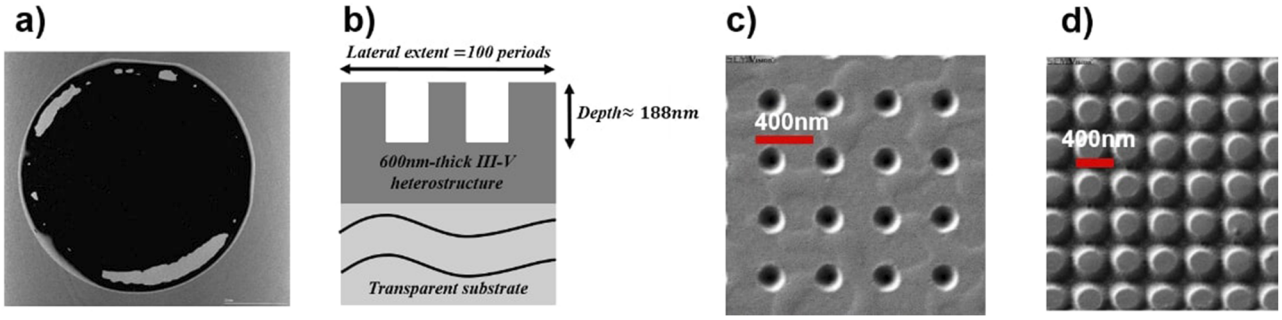

FIG. 1. (a) Scanning acoustic microscopy (SAM) image of the bonded epi-layer before substrate removal. (b) Cross section of the color-converter on the transparent substrate. Scanning electron microscopy (SEM) images of (c) holes and (d) pillars with a lattice period of 400 nm.

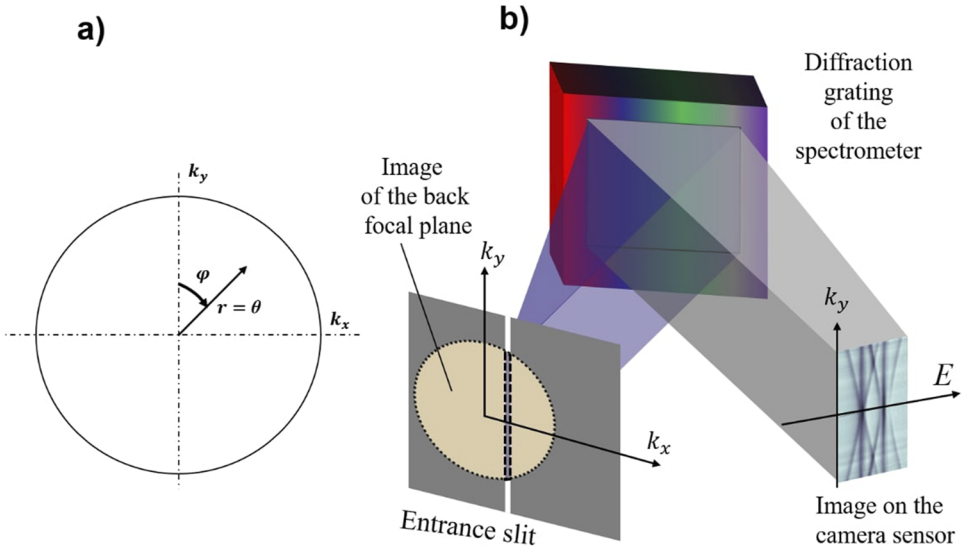

FIG. 2. (a) Image of the BFP (azimuthal farfield patterns). (b) Acquisition setup for the spectrally resolved farfield measurements.

© Author(s) 2022

III. ASSESSMENT OF THE DIRECTIONALITY OF A LIGHT EMITTER

As mentioned in Sec. I, directionality is a key FoM for some applications such as microdisplays.

The integrated intensity within the acceptance angle θ is calculated as

$$P(\theta) = \int_{\theta'=0}^{\theta'=\theta} \int_{\varphi=0}^{\varphi=2\pi} I(\theta', \varphi) \sin(\theta') d\theta' d\varphi, \quad (1)$$

where I is the emitted intensity (integrated over the whole emission spectrum), θ is the acceptance angle [apex angle of the acceptance cone related to the numerical aperture (NA) by NA = sin (θ)], and φ is the azimuthal angle.

In this framework, directionality reads as

$$D(\theta) = \frac{P(\theta)}{P(90°)}. \quad (2)$$

For a Lambertian emitter, the directionality is $D(\theta) = (\sin(\theta))^2$. In particular, it means that only 25% of the emitted light is concentrated into a cone with an apex angle of 30°.[13]

In the following, we will use the measured azimuthal farfield radiation patterns to evaluate directionality enhancement as the ratio between directionality of the PhC structures and directionality of a Lambertian emitter used as a reference. It reads as

$$\eta_D(\theta) = \frac{D_{PhC}(\theta)}{D_{lambertian}(\theta)}. \quad (3)$$

IV. RESULTS AND DISCUSSIONS

This section is organized as follows: we first deal with the azimuthal farfield emission patterns of our fabricated structures and their directionality, then the diffractive properties of the PhC are further investigated using spectrally resolved farfield patterns. Next, we take a closer look on the origin of highly directional emission using a model based on the standard transfer-matrix method with dipole source terms and the vectorial Bragg's law.

A. Azimuthal farfield radiation patterns and directionality of the CC

Figure 3 shows the measured azimuthal farfield radiation patterns of the fabricated structures, each of them normalized with its maximum value.

The farfield shapes of unpatterned CC display concentric rings with the highest emitted intensities at the periphery of the farfield shape (θ ~ 45°). Indeed, only directly emitted light inside the air cone, which exhibits a circular symmetry in the planar case,[19,27] appears in the farfield pattern.

However, for the patterned CC, the farfield shapes are more intricate. Indeed, both pattern types exhibit emission shapes where bands corresponding to the diffraction of guided Bloch-modes by the PhC are superimposed on a homogeneous background corresponding to the directly emitted light.[13,20] The previous circular symmetry is broken into a four-fold symmetry, which is inherent to the square symmetry of the PhC lattice.

For the hole-type PhC configuration, the radiation patterns strongly depend on the lattice period. For instance, while the structures with lattice periods of 400 and 450 nm reveal highly directional emission patterns with most of the diffracted light inside a cone with an apex angle of ~9° for a = 450 nm, the radiation pattern for a = 500 nm exhibits almost no diffraction close to normal incidence. For a = 550 nm, the radiation pattern is more intricate with emission close to normal incidence and at the periphery of the farfield shape.

For pillar-type structures on the other hand, there is light diffraction close to normal incidence for all lattice periods with farfield shapes different from those of hole-type PhC patterns. Particularly, for a = 500 nm, the emission pattern exhibits two sets of four diffraction bands rotated by an angle of 45°, yielding a four-branch-star-shaped pattern. This matches with the azimuthal angle difference between the ΓX- and ΓM-directions of the square lattice and, therefore, suggests that both first and second order diffraction (first and second nearest sets of four neighbors in the reciprocal lattice) contribute to the light extraction processes at this lattice period.[13,20] The same behavior can also be observed for pillars with lattice periods of 450 and 550 nm and for holes with a lattice period of 550 nm.

We use those farfield emission patterns to assess the directionality enhancement of our CC over Lambertian emission within different acceptance angles [see Eq. (3)]. The results are given in Fig. 4 on a semi-log scale. For the sake of comparison, the directionality enhancement of the unpatterned CC is also displayed.

As expected from the azimuthal farfields, directionality enhancement depends on the pattern type and the lattice period.

For holes, directionality enhancement depends only weakly on the lattice period at high acceptance angles. However, directionality enhancement becomes lattice-period dependent for decreasing acceptance angles, as a result of the strong variations of the azimuthal farfield patterns observed in Fig. 3. Although almost all lattice periods exhibit a substantial increase in directionality enhancement for decreasing acceptance angles, the optimum for holes are a = 400 nm and a = 450 nm, offering the highest directionality enhancement factors from ~2 at 49° to ~4.25 and ~4.75 close to normal incidence, respectively, as expected from their highly directional emission patterns in Fig. 3(b). The lattice period a = 500 nm, on the other hand, exhibits the lowest directionality enhancement for holes, even lower than that of the unpatterned CC, with a decrease from ~2 at 49° to less than ~1.5 at ~5° before reaching ~2.7 close to normal incidence. This is a result of the quasi-absence of light diffraction close to normal incidence in the corresponding farfield pattern (see Fig. 3). The lattice period 550 nm, on the other hand, exhibits an intermediate value of ~3.25 close to normal incidence (still higher than the unpatterned CC), as a result of the light diffraction close to normal incidence and the periphery of its farfield shape.

For pillars, directionality enhancement depends similarly on the acceptance angles with lower values for some lattice periods. However, contrary to holes, it only weakly depends on the lattice period: e.g., close to normal incidence, directionality enhancement is between ~3.4 for a = 500 nm and ~3.6 for a = 450 nm. Besides, we can note that all lattice periods exhibit higher directionality enhancement than the unpatterned reference CC.

© Author(s) 2022

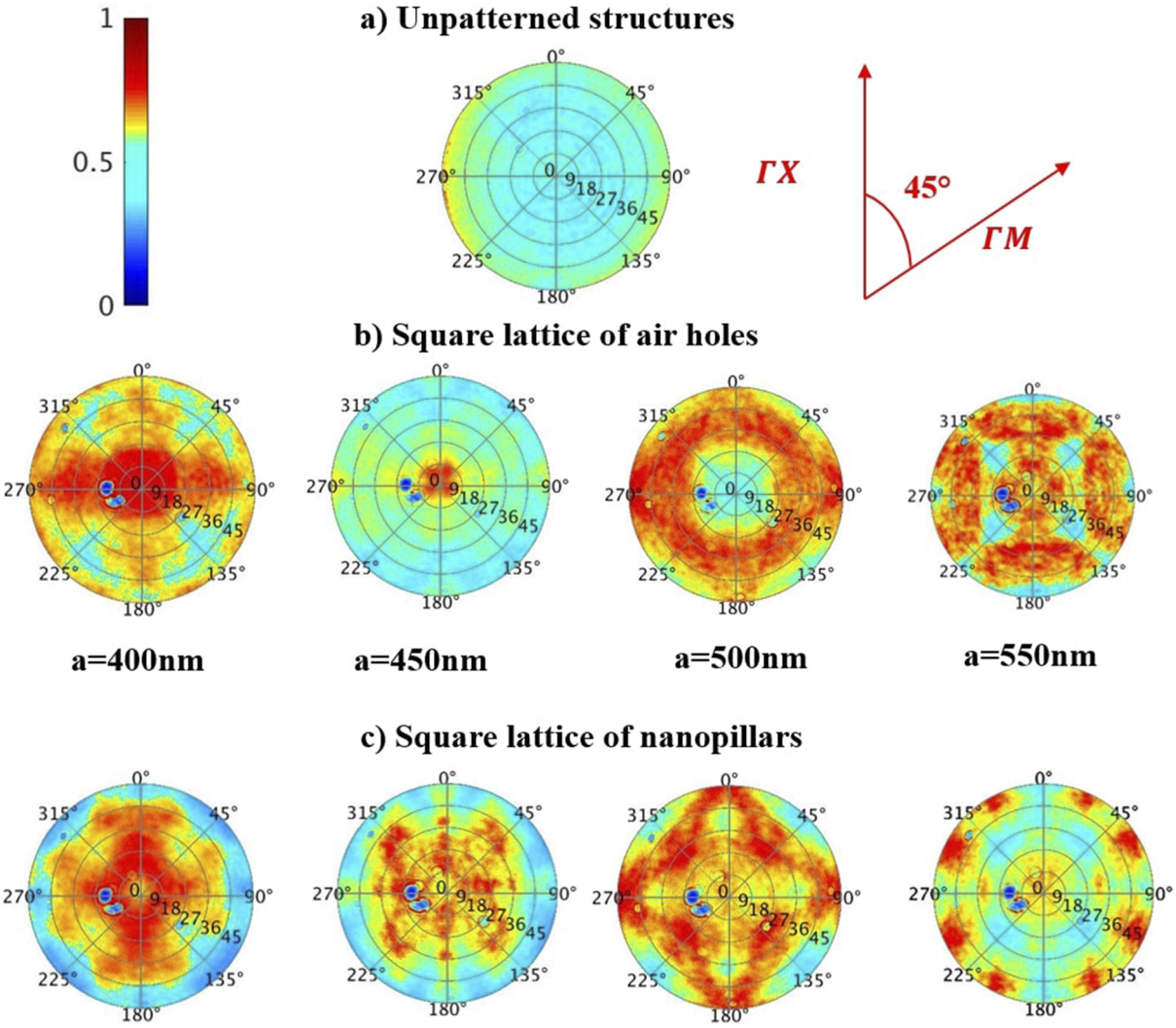

FIG. 3. Normalized azimuthal farfield radiation patterns for the (a) unpatterned CC, (b) holes, and (c) pillars.

It thus appears that by correctly choosing the pattern type and the lattice period, directionality can be significantly enhanced over Lambertian emission. For our structures, holes with lattice periods of 400 and 450 nm are the optimum, exhibiting sizable gains in directionality in the range of the measured acceptance angles (up to ×4.75), particularly close to normal incidence, which can be of major interest for applications such as microdisplays.[12]

We can also note a peculiar behavior of holes with a lattice period of 500 nm whose directionality enhancement is even lower than that of the unpatterned reference for low acceptance angles as a result of the quasi-absence of light diffraction close to normal incidence. For the same lattice type and the same lattice period, pillars did not exhibit this type of behavior. This latter point will be further analyzed in Subsection IV B.

B. Spectrally resolved farfields

To further investigate the diffractive properties of the PhC structures and their impact on the directionality of our CC, we use spectrally resolved farfields.[28] The experimental setup is described in Sec. II. A polarizer was used to selectively detect *s*- and *p*-polarized light.[29] For the sake of comparison, similar measurements were also performed on the unpatterned CC.

Figure 5 displays the results from the unpatterned CC for both light polarizations in a λ–θ representation, θ being the acceptance angle as described in Fig. 2, each of them being normalized with its maximum value. As expected, the farfield shapes are polarization-dependent as a result of the polarization dependency of the directly emitted light inside the air cone.[30,31]

© Author(s) 2022

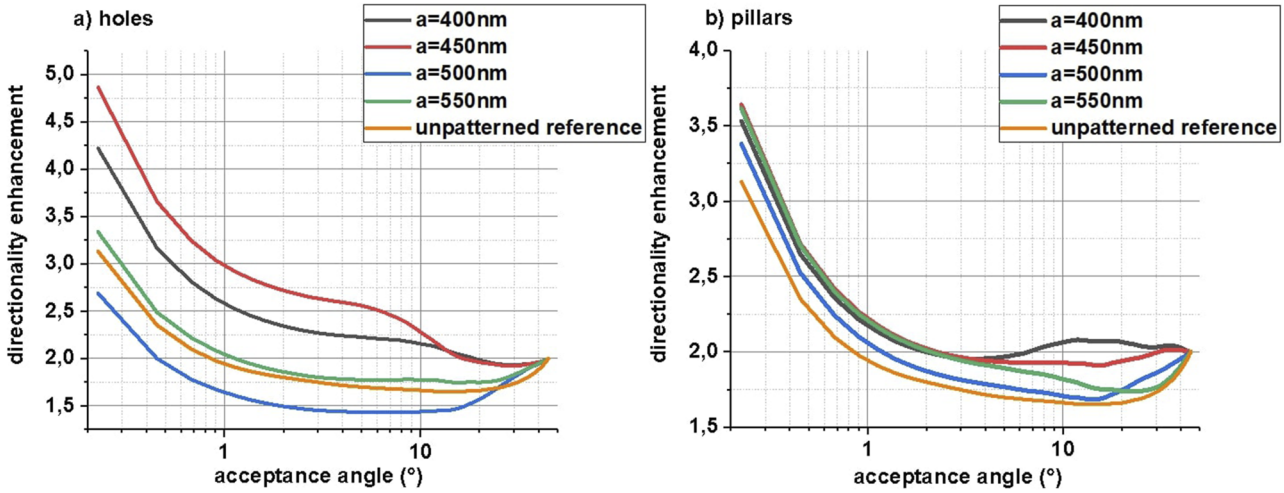

FIG. 4. Directionality enhancement for PhC-based CC over Lambertian emission for (a) holes and (b) pillars.

From the *p*-polarized light, a quite homogeneous farfield shape arises except for high intensity broad lobes around θ = ±45°. These lobes become more visible for *s*-polarized light and correspond to angular modulations of the internal emission inside the air cone due to interference effects inside the CC cavity.[20]

Figures 6 and 7 on the other hand show the normalized spectrally resolved farfield patterns along the ΓX-direction of holes and pillars, respectively. Contrary to the unpatterned CC, oblique bands are superimposed on top of the directly emitted light. Each of them

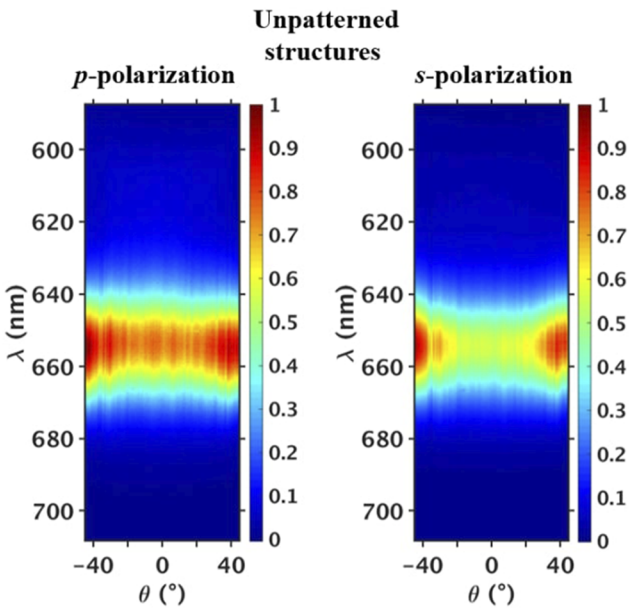

FIG. 5. Normalized spectrally resolved farfields from the unpatterned CC for *s*- and *p*-polarized light.

corresponds to the diffraction of a guided Bloch-mode into air by the PhC patterns according to Bragg's law; therefore, their angular position shifts with the wavelength.[20]

Let us recall that the CC acts as a multimode waveguide (~600 nm-thick). Due to the thin nature of the epitaxial film, all those guided modes are prone to efficient interaction with the PhC patterns and diffraction into air,[19] resulting into intricate spectrally resolved farfield patterns.

For holes, the farfield patterns are strongly lattice-period dependent. The lattice period a = 400 nm, for instance, can exhibit farfield shapes with a strong light diffraction close to normal incidence, particularly for the p-polarization. We can see that this arises from the most intense diffraction band crossing the Γ-point close to the peak emission wavelength. Similar conclusions hold for a = 450 nm, which resulted in the large directionality enhancement factors obtained previously for those two lattice periods. For a = 500 nm, on the other hand, there is a quasi-absence of guided light diffraction close to normal incidence for both polarizations. Looking closely at the most intense bands of the farfield patterns at this lattice period, we can note that this low light diffraction close to normal incidence arises from a slight detuning between those bands at the Γ-point and the emission spectrum. Therefore, they cross the Γ-point at the short-wavelength edge of the emission spectrum (near λ = 634 nm, with low PL intensity), resulting in the lowest directionality enhancement factors. The lattice period 550 nm exhibits farfield shapes with most intense bands overlapping the emission spectrum away from the *Γ*-point, near θ = ±20°, which is consistent with the azimuthal farfield shapes in Fig. 3(b). Still, it results in intermediate values of directionality enhancement factors since some of the less intense bands cross the *Γ*-point close to the peak emission wavelength.

For pillar-type structures, on the other hand, there is light diffraction close to normal incidence for all lattice periods and light polarizations with farfield shapes different from those of holes. Particularly, for a = 500 nm, there can be a strong light diffraction

© Author(s) 2022

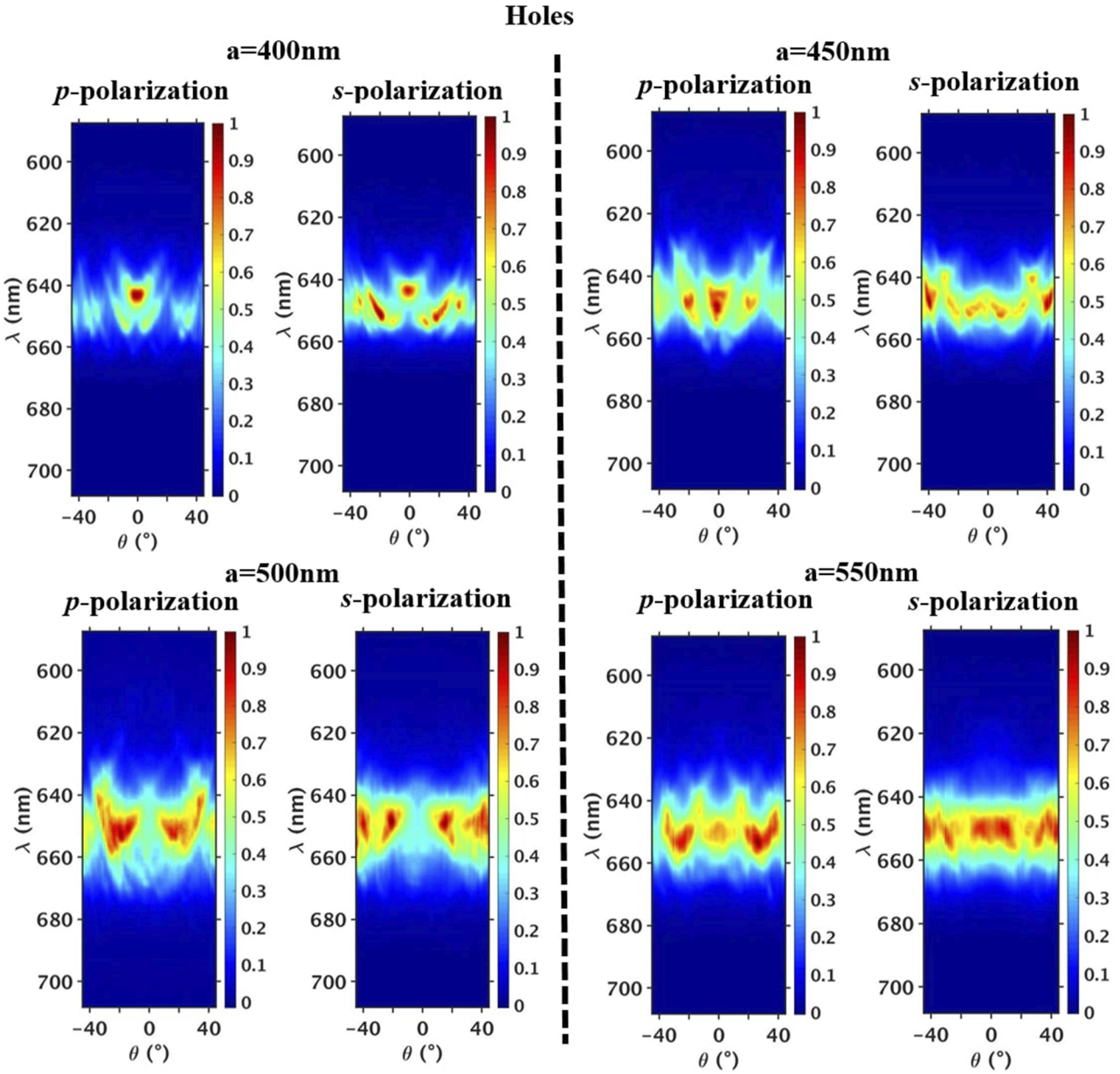

FIG. 6. Normalized spectrally resolved farfields for the square lattice of air holes with lattice periods from a = 400 nm to a = 550 nm and in the ΓX-direction. Both *s*- and *p*-polarized light are measured.

close to normal incidence as opposed to holes with a lattice period of 500 nm, which exhibited an absence of light diffraction near the Γ-point close to the peak emission wavelength. The fact that at the same lattice period some of the diffracted bands of pillars can cross the Γ-point close to the peak emission wavelength suggests that pillar-based CC and hole-based CC have different effective index distribution inside their cavity, as we will see in Sec. IV C. Besides, we notice that the diffraction bands for pillars are broader in the $k_{//}$-space (corresponding to the θ-axis in Figs. 6 and 7) than those of holes, which makes them trickier to distinguish. Indeed, the stronger coupling between the guided Bloch-modes and the air radiated modes for pillars results in shorter extraction lengths.[19] Since for a given guided Bloch mode the broadening in the $k_{//}$-space is inversely proportional to its extraction length[32] $[\Delta k_{//} \sim (L_{extraction})^{-1}]$, the latter yields broader diffraction bands for pillars. Due to those broader bands, the farfield shapes of pillars

© Author(s) 2022

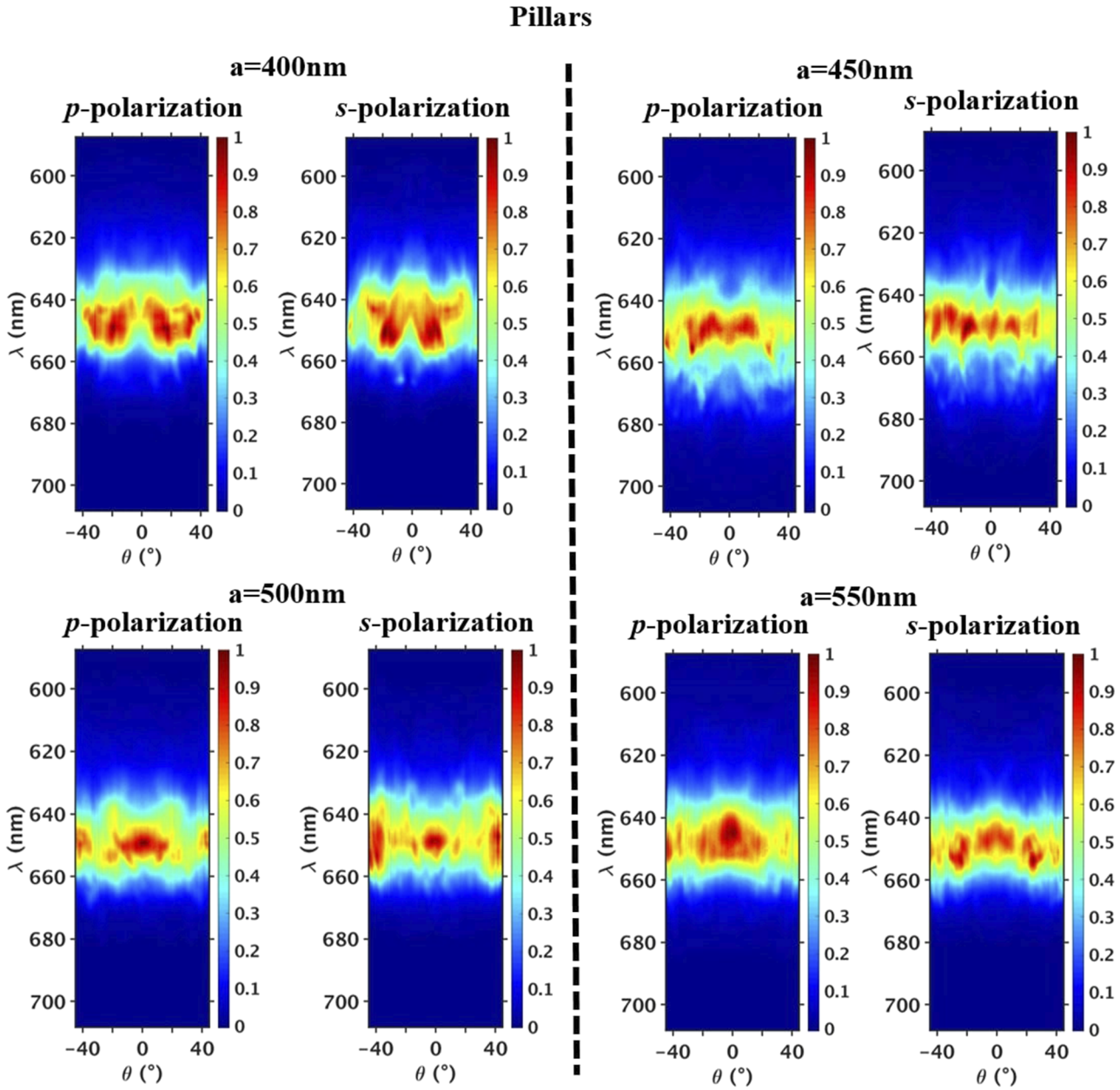

FIG. 7. Normalized spectrally resolved farfields for the square lattice of nanopillars with lattice periods from a = 400 nm to a = 550 nm and in the ΓX-direction. Both s- and p-polarized light are measured.

can exhibit strong light diffraction within a broader angular range, resulting in lower directionality than for holes close to normal incidence as previously observed.

So far, it appears that the emission directionality is ultimately not only determined by light diffraction according to Bragg's law, but also depends on the relative intensities of the diffracted bands arising from each mode. The highest directionality is achieved when the lattice period is tuned so that the most intense diffraction bands cross the Γ-point close the peak emission wavelength. This latter point will be further investigated in Sec. IV C.

C. Coupling mechanisms near the Γ-point

We have previously seen that the highest directionality is achieved when the lattice period is tuned so that the most intense

© Author(s) 2022

diffraction bands cross the Γ-point close to the peak emission wavelength. In this section, we will further investigate what mostly sets the intensity of the diffracted bands, before coming back to how to properly tune the lattice period to achieve highly directional emission. Subsequently, we identify the most intense bands of some of the farfield patterns in Fig. 6 and highlight novel design guidelines for highly directional emission from the color converters (CC).

1. Impact of spontaneous emission distribution on the directionality

As previously mentioned, directionality depends on the relative intensities of the diffraction bands arising from each mode. This latter quantity will ultimately depend on the fraction of the guided energy carried by the mode as compared to the other modes.[33]

To investigate how the emitted light is distributed among the guided modes in our CC, we performed numerical simulations using a well-established model based on the standard transfer-matrix method with dipole source terms.[34–38] This model takes as entries structural and optical parameters and provides us with the internal distribution of the light emission as a function of the effective indices of the modes.

Figure 8 depicts the schematics of the model used for our CC with the corresponding optical and structural parameters for each layer taken from the literature.[39–41] The PhC patterns are treated as a homogeneous layer with a filling-factor-weighted average refractive index, which holds for weakly corrugated gratings.[42–44] More details about the aforementioned model can be found in Refs. 30, 31, and 35.

Figure 9 displays the internal distribution of light emission as a function of the effective index for a CC based on holes with a lattice of 400 nm (see Ref. 19 for the corresponding optogeometrical parameters).

As can be seen in Fig. 9, the radiation dynamics depends on the light polarization, which explains the polarization-dependency of the farfield shapes in Figs. 5–7. Light emitted inside the CC can couple to different types of modes.[37,38] A fraction of the emitted light, which is in the air cone ($n_{eff} < 1$), directly radiates in the air or toward the substrate. This is the so-called directly emitted light and features the background farfield observed in Figs. 6 and 7. Another fraction of the emitted light is propagative in the transparent substrate but not in air ($1 < n_{eff} < 1.45$). Most of the emitted light excite the available guided modes supported by the CC, which are represented by sharp peaks outside the air and substrate cones ($n_{eff} \geq 1.45$).

The intensity of those peaks sets the fraction of the guided energy carried by each mode, which we will refer to as the photonic weight of the mode. If we note the peak intensity of the guided mode labeled i, P_i, and its angular position, θ_i, then by taking into account the solid angle, the fraction of the guided energy carried by the mode (its photonic weight) can be evaluated by $P_i \sin(\theta_i)/\sum_j P_j \sin(\theta_j)$. In Fig. 9, the corresponding photonic weights of each of the guided modes are given in the bar plot on the bottom. For instance, for p-polarization, the guided mode with $n_{eff} = 1.6$ carries more half of the guided energy. Therefore, if the lattice period is tuned so that the band arising from this mode crosses the Γ-point close to the peak emission wavelength, then the resulting spectrally resolved farfield patterns should be highly directional.

Let us note that, since pillars have far higher air filling factor than holes,[19] their guided mode distribution is different from that of holes, which explains the different farfield shapes previously observed for the same lattice period when we change the lattice pattern from holes to pillars.

It thus appears that the relative intensity of the diffracted bands depends on the spontaneous emission distribution between the guided modes supported by the CC. Each guided mode has a photonic weight, which corresponds to the fraction of the guided energy carried by this mode and can be quantified. In the following, we will discuss how to properly tune the lattice period so that those modes with high photonic weights give rise to diffraction bands that cross the Γ-point close to the peak emission wavelength to achieve highly directional emission.

2. Tuning the lattice period for highly directional emission

We have seen that directionality close to normal incidence depends on how the lattice period is tuned to target the suitable

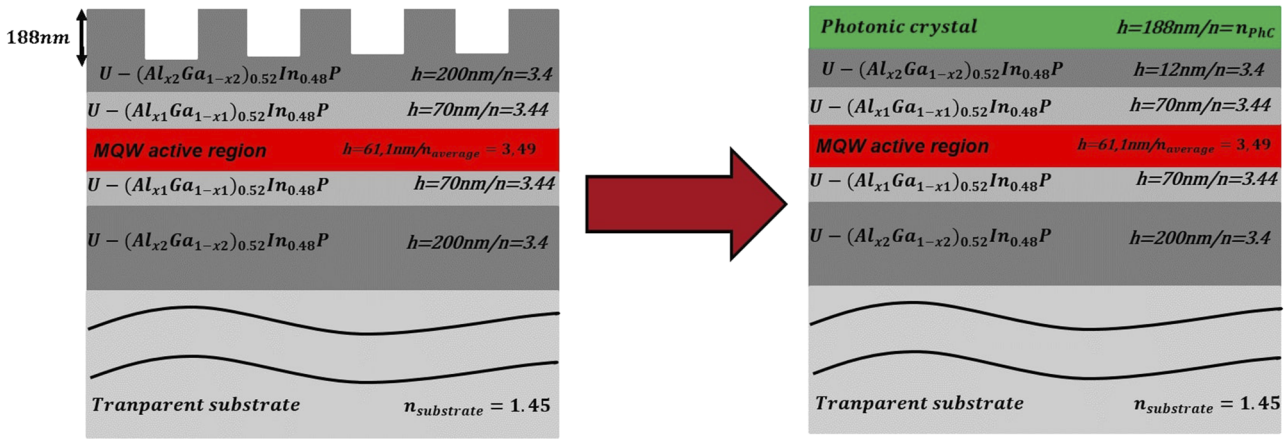

FIG. 8. Schematics of the model used for the numerical simulations.

© Author(s) 2022

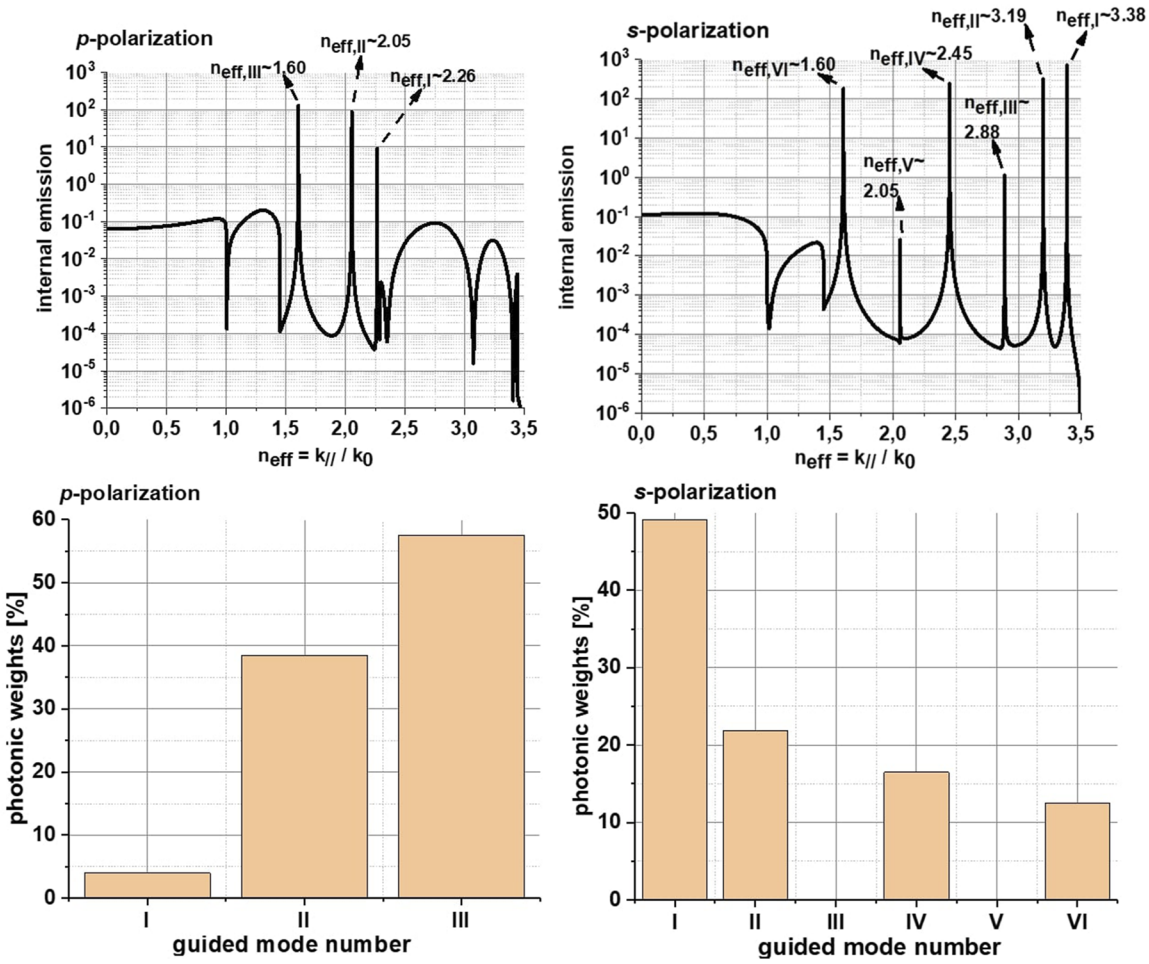

FIG. 9. Internal emission per unit solid angle as a function of the effective index for PhC-based CC with holes with a = 400 nm and the corresponding photonic weights of each mode for both s- and p-polarization.

mode at the Γ-point. To better understand how the lattice period impacts the diffracted effective indices, we use the 2D grating equation derived from the vectorial Bragg's law,[45–48] which, applied to the case of square lattices diffracting light into air, reads as

$$\sin(\theta_{mn})\cos(\varphi_{mn}) = n_{eff\,i}\cos(\varphi_i) + m\frac{\lambda}{a}, \tag{4}$$

$$\sin(\theta_{mn})\sin(\varphi_{mn}) = n_{eff\,i}\sin(\varphi_i) + n\frac{\lambda}{a}, \tag{5}$$

where n_{effi} is the effective index of the incident guided mode, θ_{mn} and φ_{mn} are the polar and azimuthal angles of the diffracted wave with m and n corresponding to the diffracted orders, and a is the lattice period. In this framework, we can find after some calculations (see Note III in the supplementary material for more details) that the effective indices coupled to the Γ-point ($\theta_{mn} = 0°$) satisfy the following equations (for odd and even diffraction orders, respectively):

$$a = m\frac{\lambda}{n_{eff\,i}}, \tag{6}$$

$$a = m\frac{\lambda}{n_{eff\,i}}\sqrt{2}. \tag{7}$$

It thus appears that for a given effective index corresponding to a mode with a high photonic weight and at a given peak emission wavelength, the lattice period has to be properly tuned so that it matches Eqs. (6) and (7) based on the simple band folding mechanisms. We have also seen in the previous sections that a slight detuning between the most intense bands at the Γ-point and the emission spectrum can lead to a large decrease in the directionality (see holes with a = 500 nm).

© Author(s) 2022

In the following, we will use all the previous considerations to further investigate the origins of the highly directional emission observed for holes with a = 400 nm.

3. Photonic band-structure analysis

We wish to further investigate the origins of the highly directional emission for holes with a = 400 nm using the previous considerations. The measured photonic band structure is directly obtained from the spectrally resolved farfield patterns in Fig. 6 by converting the wavelength and angle into the normalized frequency and in-plane wave vectors, respectively.[43,47] The resulting photonic band structure for *p*- and *s*-polarized light from holes with a = 400 nm is displayed in Fig. 10.

For *p*- and *s*-polarized light, we have identified the intense band crossing the Γ-point at $a/\lambda \approx 0.62$ to be the guided mode with $n_{eff} = 1.6$ arising from the first diffraction order (see Note IV in the supplementary material for more details on the identification procedure). The corresponding calculated band using the plane-wave expansion (PWE) algorithm in the free-photon approximation regime (the white dashed line in Fig. 10) is superimposed on the measured band structures. The calculated bands are in good agreement with the measured ones, which confirms our previous considerations.

We can also note the presence of a second closely spaced parallel band arising for both *s*- and *p*-polarized light. Indeed, despite the weakly corrugated regime, the PhC pattern will induce for each guided mode a slight modal index-contrast[47,49] giving rise to two different modes with very close effective indices. This slight index-contrast will result in a mini-band-splitting that can be modeled using the standard coupled-mode theory. In this framework, the spectral width between the two resulting bands reads as[50,51]

$$\Delta u_{ab} = \frac{a}{2\pi} \times \frac{4\kappa_{ext}}{n_{effa} + n_{effb}}. \quad (8)$$

Here, u is the normalized frequency, Δu_{ab} accounts for the spectral width between the two bands, κ_{ext} is the modal coupling constant between the Bloch mode and the air radiated modes, and n_{effa} and n_{effb} are the effective indices of the two modes. The previous free-photon approximation needs then to be corrected using coupled-mode theory. For *p*-polarization, we found that the second diffracted band (labeled "b") crosses the Γ-point at $u_b = 0.61$, which gives $n_{effb} = 1.64$ using Eq. (6) and $\Delta u_{ab} = 0.01$. The corresponding calculated bands using PWE (the black dashed line in Fig. 10) are superimposed on the measured ones showing very good agreement, which supports our analysis. Similar treatments are also performed for *s*-polarization as displayed in Fig. 10.

We can note that using the values extracted from the measured band structure, we obtain a modal coupling constant of $\kappa_{ext} \approx 0.1\ \mu m^{-1}$, which is consistent with the values found in Ref. 19 using another approach.

Thus, we have noted that the spectrally resolved farfield patterns in Fig. 6 for holes with a = 400 nm are dominated at the Γ-point by the guided mode with $n_{eff} \approx 1.6$ arising from the first diffraction order. For *p*-polarization, we have evaluated that this mode can carry more than half of the guided energy (see Fig. 9). Since the lattice period is properly tuned so that the corresponding band crosses the Γ-point close to the peak emission wavelength, we obtain a highly directional emission with a strong light diffraction at the Γ-point.

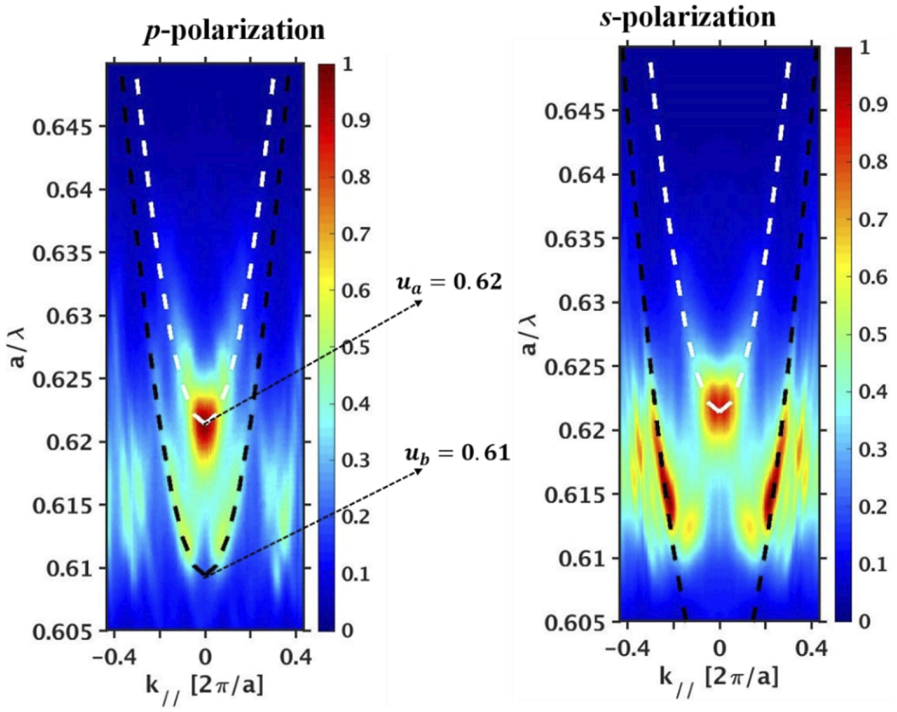

FIG. 10. Measured photonic band structures for holes with a = 400 nm for p- and s-polarized light. Calculated band structures for modes with $n_{effa} = 1.6$ (white dashed lines) and with $n_{effb} = 1.64$ (black dashed lines for p-polarization) and $n_{effb} = 1.67$ for s-polarization.

© Author(s) 2022

We have found that the guided energy for *s*-polarized light on the other hand is shared among more modes, which tends to mitigate the previously mentioned effect. This results in a less directional emission close to normal incidence than for *p*-polarization, as evidenced by some very intense bands away from the Γ-point, near $\theta = \pm 30^{\circ}$ (see Fig. 6). This highlights the major role played by the spontaneous emission distribution between the guided modes on the directionality.

D. Design guidelines and light extraction efficiency enhancement

On a device point of view, there are two major design rules that can be set from the previous analyses.

On the one hand, we have seen that despite multimode light extraction, large directionality enhancement factors over Lambertian emission can be achieved when the lattice period is properly tuned so that the most intense diffraction bands cross the Γ-point close to the peak emission wavelength. This requires simultaneously a control of the spontaneous emission distribution between the guided modes to identify the guided modes with the highest photonic weights (carrying a large fraction of the guided energy) and an optimized choice of the lattice period based on the band-folding mechanism in a 2D configuration as explained in the previous sections.

On the other hand, we have seen that with lattice periods of 400 and 450 nm, directionality can be enhanced by factors up to four times over a Lambertian emission. This could eliminate the need to reach very low lattice periods to target low order modes with the first diffraction order.[22,52] This is of particular interest because by choosing lattice periods higher than 400 nm, we also allow all the guided modes supported by the CC to be prone to light extraction.[19] Thus, directionality can be properly tuned following the methodology described above while maintaining high LEE.

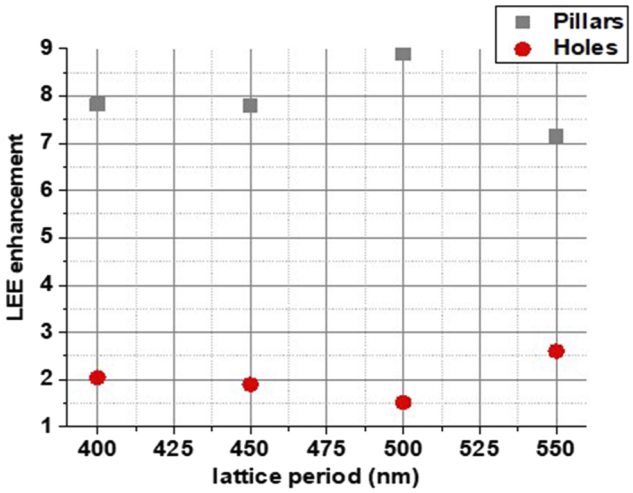

FIG. 11. Light extraction efficiency enhancement as a function of the lattice periods for holes and pillars.

Figure 11 displays the measured LEE enhancement factors over the unpatterned reference, which have been evaluated using the micro-photoluminescence setup described in Ref. 19 with NA = 0.9. It shows that LEE enhancement only slightly varies as a function of the lattice period for both holes and pillars. We can note that the highest enhancement factors are obtained for pillars (up to ×9) because hole-type structures tend to diffract more light toward the transparent substrate than pillar-type structures.[19] Besides, the possibility of using higher lattice periods can be of major interest on a technological point of view since they are more reachable by standard deep-UV lithography processes than lower ones. These considerations could give novel insights regarding the design of highly directional emission from MQW color converters for microdisplay applications and others.

Thus, it appears that in our structures, the radiation patterns can be properly shaped to achieve highly directional emission following the methodology described above, while maintaining high LEE. The coupling to external optical systems with very limited numerical apertures can, therefore, be optimized, which is of major interest for applications such as microdisplays.

V. CONCLUSION

We have provided novel design guidelines for highly directional emission from PhC-based AlGaInP/InGaP MQW color converters (CC) in a thin-film geometry through an in-depth analysis of the measured azimuthal and spectrally resolved farfield emission patterns and a modal analysis based on a herein-developed model for quantifying the spontaneous emission distribution between guided modes. PhCs with different optogeometrical parameters were etched into stand-alone CC bonded on a transparent substrate using a high-bonding-yield oxide-mediated molecular bonding.

Analyses of spectrally resolved farfield patterns coupled to the herein-developed model help us in conducting a modal analysis near the Γ-point and highlighting a fundamental condition necessary to achieve highly directional emission in such color converters: the lattice period needs to be properly tuned so that the most intense diffraction bands cross the Γ-point close to the peak emission wavelength. This requires simultaneously a control of the spontaneous emission distribution between the guided modes (which has been quantified) to identify the guided modes with the highest photonic weights (carrying a large fraction of the guided energy) and an optimized choice of the lattice period based on the band-folding mechanism in a 2D configuration.

The fabricated color-converters can exhibit directionality up to ~5 times higher than that of Lambertian emitters close to normal incidence.

We believe that all the novel insights set through our analyses could eliminate the need for additional external optics and, therefore, pave the way for the use of MQW CC to achieve compact full-color microdisplays on a single wafer.

Current and future studies are mainly focused on investigating all the steps required for the implementation of the herein fabricated color converters on blue or green micro-LED arrays.

© Author(s) 2022

SUPPLEMENTARY MATERIAL

Details about the fabrication process, the experimental setup, Bragg's law for coupling to the Γ-point, and the modal identification process are provided in the supplementary material.

ACKNOWLEDGMENTS

The authors would like to thank A. Ghazouani and N. Olivier for their help on device fabrication and E.Quesnel for insightful discussions. The authors acknowledge funding from the Clean Sky 2 Joint Undertaking under the European Union's Horizon 2020 research and innovation program under Grant Agreement No. 755497.

AUTHOR DECLARATIONS

Conflict of Interest

The authors have no conflicts to disclose.

DATA AVAILABILITY

The data that support the findings of this study are available from the corresponding author upon reasonable request.

REFERENCES

[1] S. Li, L. Wang, N. Hirosaki, and R. J. Xie, Laser Photonics Rev. **12**, 1800173 (2018).
[2] S. Gorsky, R. Zhang, A. Gok, R. Wang, K. Kebede, A. Lenef, M. Raukas, and L. Dal Negro, APL Photonics **3**, 126103 (2018).
[3] S. Y. Lee, G. Lee, D. Y. Kim, S. H. Jang, I. Choi, J. Park, H.-K. Park, J. W. Jung, K. H. Cho, and J. Choi, APL Photonics **6**, 056104 (2021).
[4] J. M. M. Santos, B. E. Jones, P. J. Schlosser, S. Watson, J. Herrnsdorf, B. Guilhabert, J. J. D. McKendry, J. De Jesus, T. A. Garcia, M. C. Tamargo, A. E. Kelly, J. E. Hastie, N. Laurand, and M. D. Dawson, Semicond. Sci. Technol. **30**, 035012 (2015).
[5] Y. Yin, W. Peng, J. Geng, X. Bai, M. Duan, Y. Wu, J. Hou, D. Li, J. Hwang, X. Zhang, and H. Meng, SID Symp. Dig. Tech. Pap. **52**, 244 (2021).
[6] E. Quesnel, A. Suhm, M. Consonni, M. Reymermier, G. Lorin, C. Laugier, M. Tournaire, P. Le Maitre, A. Lagrange, B. Racine, M. D'Amico, and E. Cao, Opt. Express **29**, 20498 (2021).
[7] B. Huang, E. Chen, L. Sun, and T. Guo, Opt. Laser Technol. **145**, 107486 (2022).
[8] E. Quesnel, A. Lagrange, M. Vigier, M. Consonni, M. Tournaire, V. Le Marchand, A. Suhm, P. Demars, J. C. Pillet, B. Ben Bakir, N. Olivier, E. Feltin, J. M. Lamy, M. D'Amico, E. Cao, G. Haas, L. Charrier, and P. Coni, J. Soc. Inf. Disp. **29**, 3 (2021).
[9] J. Osinski and P. Palomaki, SID Symp. Dig. Tech. Pap. **50**, 34 (2019).
[10] S. Han, C. Xu, H. Li, S. Liu, H. Xu, Y. Zhu, A. Fang, and X. Wang, Opt. Mater. **114**, 110860 (2021).
[11] T. A. Truong, L. M. Campos, E. Matioli, I. Meinel, C. J. Hawker, C. Weisbuch, and P. M. Petroff, Appl. Phys. Lett. **94**, 023101 (2009).
[12] X. Fu, Y. Mehta, Y. A. Chen, L. Lei, L. Zhu, N. Barange, Q. Dong, S. Yin, J. Mendes, S. He, R. Gogusetti, C. H. Chang, and F. So, Adv. Mater. **33**, 2006801 (2021).
[13] K. Bergenek, C. Wiesmann, H. Zull, C. Rumbolz, R. Wirth, N. Linder, K. Streubel, and T. F. Krauss, Proc. SPIE **7231**, 72310C (2009).
[14] M. Boroditsky, T. F. Krauss, R. Coccioli, R. Vrijen, R. Bhat, and E. Yablonovitch, Appl. Phys. Lett. **75**, 1036 (1999).
[15] X. Tang, L. Han, Z. Ma, Z. Deng, Y. Jiang, W. Wang, H. Chen, C. Du, and H. Jia, Opt. Express **29**, 5993 (2021).
[16] B. Jain, R. T. Velpula, M. Tumuna, H. Q. T. Bui, J. Jude, T. T. Pham, T. van Le, A. V. Hoang, R. Wang, H. Pham, and T. Nguyen, Opt. Express **28**, 22908 (2020).
[17] X. Liu, K. Mashooq, T. Szkopek, and Z. Mi, IEEE Photonics J. **10**, 4501211 (2018).
[18] A. David, T. Fujii, B. Moran, S. Nakamura, S. P. DenBaars, C. Weisbuch, and H. Benisty, Appl. Phys. Lett. **88**, 133514 (2006).
[19] A. Ndiaye, A. Ghazouani, C. Seassal, E. Drouard, N. Olivier, and B. B. Bakir, Opt. Express **29**, 35965 (2021).
[20] J. J. Wierer, A. David, and M. M. Megens, Nat. Photonics **3**, 163 (2009).
[21] K. Bergenek, Ch. Wiesmann, H. Zull, R. Wirth, P. Sundgren, N. Linder, K. Streubel, and T. F. Krauss, Appl. Phys. Lett. **93**, 231109 (2008).
[22] K. Bergenek, Ch. Wiesmann, R. Wirth, L. O'Faolain, N. Linder, K. Streubel, and T. F. Krauss, Appl. Phys. Lett. **93**, 041105 (2008).
[23] A. Maimone and J. Wang, ACM Trans. Graphics **39**, 67 (2020).
[24] H. Duprez, A. Descos, T. Ferrotti, C. Sciancalepore, C. Jany, K. Hassan, C. Seassal, S. Menezo, and B. Ben Bakir, Opt. Express **23**, 8489 (2015).
[25] R. Wagner, L. Heerklotz, N. Kortenbruck, and F. Cichos, Appl. Phys. Lett. **101**, 081904 (2012).
[26] Y. Mohtashami, R. A. DeCrescent, L. K. Heki, P. P. Iyer, N. A. Butakov, M. S. Wong, A. Alhassan, W. J. Mitchell, S. Nakamura, S. P. DenBaars, and J. A. Schuller, Nat. Commun. **12**, 3591 (2021).
[27] Q. Jiao, Z. Chen, Y. Feng, S. Li, S. Jiang, J. Li, Y. Chen, T. Yu, X. Kang, B. Shen, and G. Zhang, Nanoscale Res. Lett. **11**, 340 (2016).
[28] K. Bergenek, C. Wiesmann, H. Zull, C. Rumbolz, R. Wirth, N. Linder, K. Streubel, and T. F. Krauss, IEEE J. Quantum Electron. **45**, 1517 (2009).
[29] C.-F. Lai, J.-Y. Chi, H.-C. Kuo, H.-H. Yen, C.-E. Lee, C.-H. Chao, H.-T. Hsueh, and W.-Y. Yeh, Opt. Express **17**, 8795 (2009).
[30] H. Benisty, H. De Neve, and C. Weisbuch, IEEE J. Quantum Electron. **34**, 1612 (1998).
[31] H. Benisty, H. De Neve, and C. Weisbuch, IEEE J. Quantum Electron. **34**, 1632 (1998).
[32] E. Matioli, B. Fleury, E. Rangel, E. Hu, J. Speck, and C. Weisbuch, J. Appl. Phys. **107**, 053114 (2010).
[33] C. Wiesmann, K. Bergenek, R. Houdre, R. P. Stanley, N. Linder, and U. T. Schwarz, IEEE J. Quantum Electron. **45**, 1273 (2009).
[34] M. Born, E. Wolf, A. B. Bhatia, P. C. Clemmow, D. Gabor, A. R. Stokes, A. M. Taylor, P. A. Wayman, and W. L. Wilcock, *Principles of Optics: Electromagnetic Theory of Propagation, Interference and Diffraction of Light*, 7th ed. (Cambridge University Press, Cambridge; New York, 1999).
[35] H. Benisty, R. Stanley, and M. Mayer, J. Opt. Soc. Am. A **15**, 1192 (1998).
[36] J. Kim, K.-Y. Kim, and J. Kim, Opt. Express **27**, A1261 (2019).
[37] A. David, T. Fujii, R. Sharma, K. McGroddy, S. Nakamura, S. P. DenBaars, E. L. Hu, C. Weisbuch, and H. Benisty, Appl. Phys. Lett. **88**, 061124 (2006).
[38] E. Matioli and C. Weisbuch, J. Phys. D: Appl. Phys. **43**, 354005 (2010).
[39] S. Turcotte and M. Daraselia, J. Appl. Phys. **113**, 093103 (2013).
[40] M. Boucenna and N. Bouarissa, Optik **125**, 6611 (2014).
[41] M. F. Schubert, S. Chhajed, J. K. Kim, E. Fred Schubert, and J. Cho, Appl. Phys. Lett. **91**, 051117 (2007).
[42] C. Wiesmann, K. Bergenek, N. Linder, and U. Schwarz, Proc. SPIE **6989**, 69890L (2008).
[43] E. Rangel, E. Matioli, Y.-S. Choi, C. Weisbuch, J. S. Speck, and E. L. Hu, Appl. Phys. Lett. **98**, 081104 (2011).
[44] J. H. Schmid, P. Cheben, P. J. Bock, R. Halir, J. Lapointe, S. Janz, A. Delage, A. Densmore, J.-M. Fedeli, T. J. Hall, B. Lamontagne, R. Ma, I. Molina-Fernandez, and D.-X. Xu, IEEE Photonics J. **3**, 597 (2011).
[45] F. Falco, T. Tamir, and K. M. Leung, J. Opt. Soc. Am. A **21**, 1621 (2004).
[46] G. J. Lee and Y. M. Song, AIP Adv. **6**, 035104 (2016).

© Author(s) 2022

[47]A. David, C. Meier, R. Sharma, F. S. Diana, S. P. DenBaars, E. Hu, S. Nakamura, C. Weisbuch, and H. Benisty, Appl. Phys. Lett. **87**, 101107 (2005).
[48]C. Wiesmann, K. Bergenek, N. Linder, and U. T. Schwarz, Laser Photonics Rev. **3**, 262 (2009).
[49]C.-F. Lai, C.-H. Chao, H.-C. Kuo, H.-H. Yen, C.-E. Lee, and W.-Y. Yeh, Appl. Phys. Lett. **94**, 123106 (2009).
[50]S. Olivier, H. Benisty, C. Weisbuch, C. J. M. Smith, T. F. Krauss, and R. Houdre, Opt. Express **11**, 1490 (2003).
[51]L. A. Coldren, S. W. Corzine, and M. L. Mashanovitch, *Diode Lasers and Photonic Integrated Circuits*, 2nd ed. (Wiley, 2012).
[52]K. McGroddy, A. David, E. Matioli, M. Iza, S. Nakamura, S. DenBaars, J. S. Speck, C. Weisbuch, and E. L. Hu, Appl. Phys. Lett. **93**, 103502 (2008).

© Author(s) 2022